Super-Resolution Inversion and Reconstruction of Remote Sensing Image of Unknown Infrared Band of Interest

YAN Junhua[1,2*], *YU Liqian*[1,2], *XIA Chongxiang*[1,2], *ZHANG Qiqi*[1,2], *XU Zhenyu*[1,2], *ZHANG Yin*[1,2], *FAN Junjie*[1,2]

1. Key Laboratory of Space Photoelectric Detection and Perception (Nanjing University of Aeronautics and Astronautics), Ministry of Industry and Information Technology, Nanjing 211106, P.R.China;
2. College of Astronautics, Nanjing University of Aeronautics and Astronautics, Nanjing 211106, P.R.China

(Received 18 November 2022; revised 6 May 2023; accepted 12 June 2023)

Abstract: This paper proposes a super-resolution inversion and reconstruction algorithm for remote sensing images of unknown bands of interest. The proposed method utilizes a built-in spectral reflectance database and the existing multispectral image to achieve the accurate classification of substances through the implementation of a Gaussian hybrid clustering algorithm and correlation distance method after radiation calibration and atmospheric correction. The image mixing algorithm based on the manifold space constraint obtains the distribution of ground substances, based on which the spectral reflectance image of the unknown band of interest is reconstructed. By employing the single-window algorithm, the temperature field of low-resolution ground substances is inverted through the far-infrared image, and the Shepard interpolation algorithm is used to interpolate the low-resolution temperature field to obtain a high-resolution ground temperature field. According to the spectral reflectance and the temperature field of the ground substances, using the remote sensing link imaging model, the high-resolution remote-sensing image of unknown infrared band of interest is super-resolution inversion reconstructed. Experimental results show that the reconstructed infrared image of various scenes has a high similarity with the original scene image, which has great benefits for improving the ability of target detection and recognition.

Key words: super-resolution inversion and reconstruction; remote sensing image; ground substance distribution; spectral reflectance database; temperature field inversion and reconstruction

CLC number: TP751.1 **Document code:** A **Article ID:** 1005-1120(2023)04-0472-15

0 Introduction

The reconstruction of high-resolution remote sensing images of unknown wave bands of interest can supplement the image data of wave bands that cannot be obtained by the detector load. "Stealth" targets can be effectively detected by using infrared band images. However, due to hardware and other limiting factors, it is difficult to obtain high-resolution remote sensing images of infrared bands of interest. Consequently, accurately detecting and identifying targets becomes a formidable task. Therefore, by reconstructing high-resolution remote sensing images of unknown infrared bands of interest based on the image data of existing bands of the detector load, the target can be accurately detected and identified.

From our investigation, at present there is little research literature on reconstructing high-resolution remote sensing images of unknown bands of interest based on the inversion reconstruction of existing bands image data, except for only one document published in 2009 by Xu et al[1]. In their study, a method was proposed to generate four infrared bands multispectral images from visible light and near-infrared band images. Although the far-infrared

*Corresponding author, E-mail address: yjh9758@126.com.

How to cite this article: YAN Junhua, YU Liqian, XIA Chongxiang, et al. Super-resolution inversion and reconstruction of remote sensing image of unknown infrared band of interest[J]. Transactions of Nanjing University of Aeronautics and Astronautics, 2023, 40(4): 472-486.

http://dx.doi.org/10.16356/j.1005-1120.2023.04.008

band image can be effectively reconstructed, the image scene used in the experiment is too simple and is not a remote sensing image, and the accuracy of the generated image has not been verified. The vast majority of existing literature has proposed the methods of super-resolution reconstructing of the high-resolution remote sensing image of known bands of interest basing on the image data of known bands. The ideas of these algorithms are very instructive and can be applied to the research on the inversion and reconstruction of high-resolution remote sensing images of unknown bands of interest.

In 2011, Singh et al.[2] proposed the iterative backward projection (IBP) algorithm. By calculating the error between the simulated low-resolution image and the actual low-resolution image, a high-resolution image that better represents the actual situation was obtained via reverse iterative update. The IBP algorithm can effectively introduce the priori image information and is no longer constrained by the motion model. However, problems such as checkerboard effects, high-frequency information loss, and local minimum are prone to occur during the convergence. In 2011, Tang et al.[3] proposed a convex set projection method based on wavelet bicubic interpolation. This algorithm can combine any priori information to reduce the ringing effect near the edge of the image through bicubic interpolation and thus realizes the super-resolution reconstruction of the image. However, due to the ill-posed problem of the algorithm, the algorithm lacks stability and the reconstruction result is not unique. In 2015, Xu et al.[4] proposed a non-local self-similar priori image denoising method based on block groups, which can reduce the error caused by low-frequency noise during super-resolution reconstruction. However, the amount of calculation is large and the convergence speed is slow. In 2016, Cao et al.[5] proposed a super-resolution reconstruction algorithm with adaptive regularization coefficients. This algorithm adaptively estimates regularization parameters for each image and combines the sparse representation to perform regularized non-convex optimization of the image. As a result, it improves the image quality. In 2017, Nazren et al.[6] proposed an improved IBP algorithm. By introducing an anisotropic diffusion model, the edges of the image were enhanced to make the image smoother, which effectively solved the problem of high-frequency information loss. Due to the instability of the anisotropic diffusion model, the algorithm has higher requirements for parameter and threshold settings. In 2017, Liu et al.[7] proposed a super-resolution reconstruction algorithm that combines the similarity between images and the self-similarity of the image itself. This method can effectively reduce the error caused by noise. However, introducing the mutual similarity of image sequences as features for training requires a large amount of prior data as the training set, and the algorithm is thus less robust. In 2018, Huang et al.[8] proposed an adaptive smooth perceptual regularization factor based on low-resolution images, which iteratively updates and calculates high-resolution images based on sparse representations. This algorithm can preserve the image edges and reduce the error caused by noise to a certain extent. However, the algorithm's robustness is compromised due to the increased computational requirements associated with prioritizing edge retention. In 2018, Zhang et al.[9] proposed to use the layering function of the convolutional neural network to extract dense local features to achieve image super-reconstruction, but this algorithm only has good performance on specific data sets, hence it is less robust. In 2019, Gao et al.[10] proposed to reduce the computational complexity through several multi-scale deep neural networks, but this method heavily relies on network design. In 2019, Jiang et al.[11] proposed a GAN-based edge-enhanced network (EEGAN) for the reconstructing of high-resolution remote sensing images with clear edges, but a large remote sensing dataset is required for training. In 2021, Xiao et al.[12] proposed a time group projection fusion strategy and precise alignment module for satellite video super-resolution to improve the efficiency and accuracy of spatio-temporal information fusion. The following year, Xiao et al.[13] designed a feature interpolation module that deeply couples optical flow and multi-scale deformable convolution to predict unknown frames, and use multi-scale spatio-temporal transformers to aggregate contextual information in long-term video frames, improving tempo-

ral and spatial resolution; but neither can be applied to the generation of remote sensing images of unknown bands of interest.

This paper proposes a super-resolution inversion reconstruction algorithm for remote sensing images of unknown infrared band of interest. According to the constructed spectral reflectance database, the Gaussian hybrid clustering algorithm and correlation distance method are used to classify and identify the substances in the scene spectral reflectance image after calibration and atmospheric correction determination of multi-spectral image of known bands. The image unmixing algorithm based on the manifold space constraint is used to obtain the distribution of the ground substances in the scene. Building upon the distribution of the ground substances, the spectral reflectance image of the unknown infrared band of interest is reconstructed by inversion. The proposed algorithm utilizes far-infrared images from known bands to perform temperature inversion and reconstruction of the high-resolution ground substance temperature field distribution of unknown infrared bands of interest. By incorporating the spectral reflectance information and temperature field information of ground substances obtained through inversion, and leveraging the remote sensing imaging link model, a high-resolution remote sensing image of the unknown infrared band of interest is super-resolution inversion reconstructed.

1 Algorithm Framework

The algorithm flow of the super-resolution inversion and reconstruction of remote sensing image of unknown infrared band of interest is shown in Fig.1. It consists of two parts: The inversion reconstruction of the spectral reflectance of ground substances and the inversion reconstruction of the temperature field of ground substances.

The ground object spectral reflectance inversion reconstruction algorithm is as follows:

(1) Perform radiation calibration of the known high-resolution multispectral digital number (DN) value image to convert the DN image into a spectral radiance image[14].

(2) Perform atmospheric correction on the calibrated image[15] to remove the influence caused by the atmosphere and transform it into a spectral reflectance image with clear physical meaning.

(3) Use the Gaussian mixture clustering model to classify each pixel in the image, and inverse the ground substance category in the image by integrating the constructed ground substances spectral reflectance database.

(4) Through pixel unmixing, analyze the components of the mixed pixels, identify the specific components of the ground substances in the image, and invert the ground substance distribution of the scene image.

(5) Once the ground substance categories in the image are determined, according to the abundance matrix of the ground substance distribution of the scene image, combined with the constructed ground substance spectral reflectance database, reconstruct the ground substance spectral reflectance image of the unknown infrared band of interest.

The steps of the inversion and reconstruction of the temperature field of the ground substance algorithm are as follows:

(1) Perform radiation calibration of the known low-resolution far-infrared DN image to convert it into a spectral radiance image.

(2) Use the single-window method to invert the temperature information of each pixel in the image, and obtain the low-resolution ground substance temperature field distribution.

(3) The low-resolution ground substance temperature field is super-resolution reconstructed using the Shedebe interpolation method to obtain the high-resolution ground substance temperature field distribution.

By integrating the inversion-reconstructed ground substance's spectral reflectance image and the high-resolution ground substance temperature field distribution of the unknown infrared band, along with the remote sensing imaging link model, a high-resolution spectral radiance image of the unknown infrared band is successfully reconstructed, thus achieving the super-resolution inversion reconstruction of the remote sensing image.

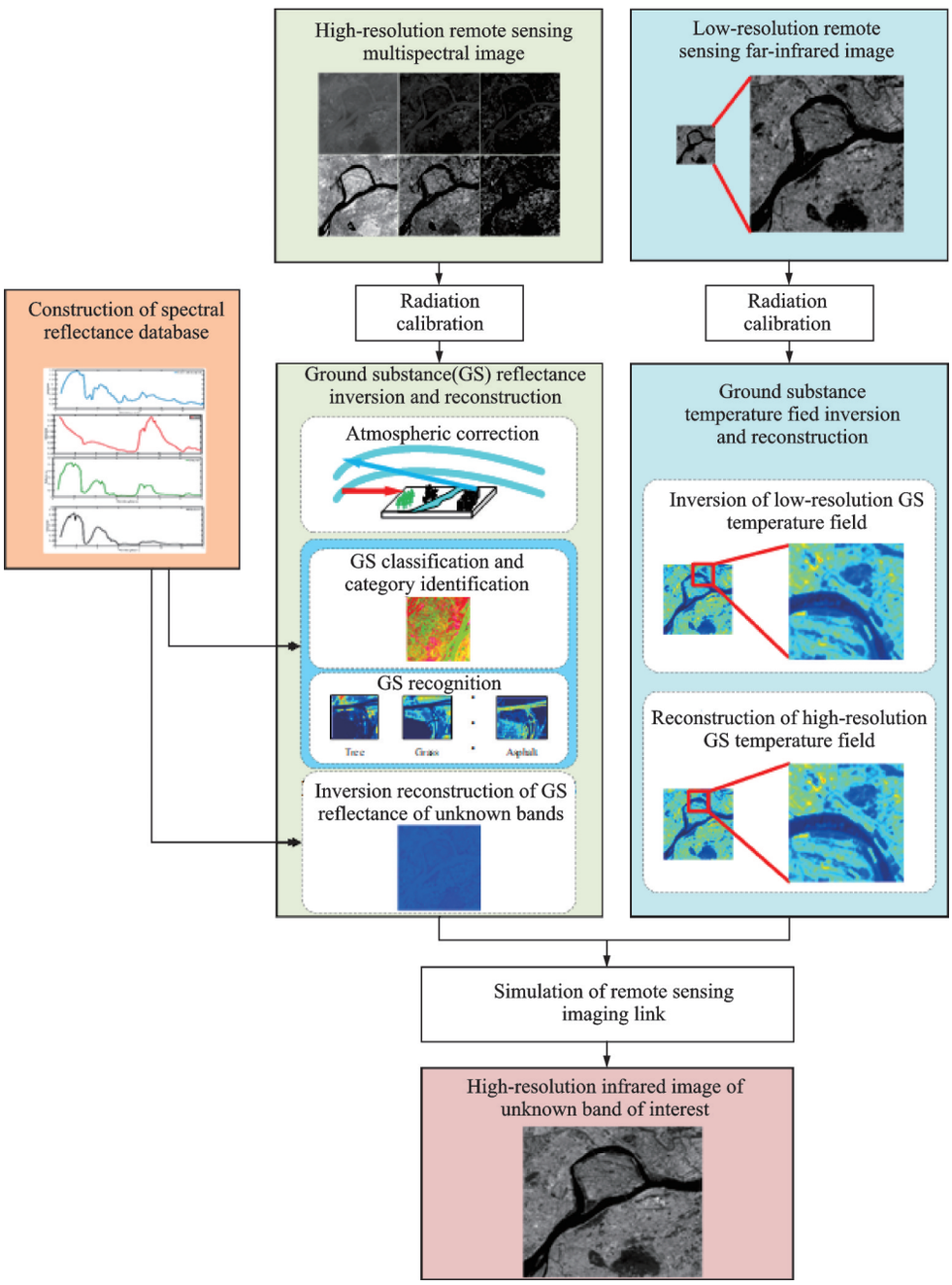

Fig.1 Algorithm flow of super-resolution inversion and reconstruction of remote sensing image of unknown infrared band of interest

2 Inversion and Reconstruction of Spectral Reflectance of Ground Substances

Spectral reflectivity is an intrinsic property of a substance and it is determined by the type of substance and the wavelength band it reflects. Using the ground substance spectral reflectance images of known bands and the spectral reflectance databases, the types and distribution of ground substances in the scene can be identified and inverted. Based on the types and distributions of ground substances in the scene and the spectral reflectance databases, the ground substance spectral reflectance image of an unknown band of interest can be reconstructed.

2.1 Construction of spectral reflectance database

The existing databases of ground substance spectral reflectance cannot comprehensively cover all substances. It is necessary to add the spectral re-

flectance of the substance of interest, and at the same time supplement the bands of substances with a narrow wavelength range, so as to accurately determine the distribution of ground substances and invert the ground substance spectral reflectance of the unknown band of interest. In this article, a spectral reflectance database is constructed, consisting of three widely used digital ground substance spectral reflectance databases and a new database (NUAA database) created by the research team. The NUAA database includes 22 types of substances, such as water bodies, artificial targets, and metal minerals. Wavebands have been supplemented to this database based on the information from the three existing databases. The spectral reflectance database is shown in Table 1.

Table 1 Spectral reflectance databases

Source database	Number of substance	Wavelength /μm	Containing substance
USGS(US Geological Survey)	131	0.2—3.0 0.4—14.0	Rock, mineral
JPL(NASA Jet Propulsion Laboratory)	1 464	0.4—2.5 0.4—25.0	Rocks, minerals, meteorite, moon
JHU(Johns Hopkins University)	826	0.4—14.0	Vegetation, soil, water bodies, snow and ice, artificial targets
NUAA(Nanjing University of Aeronautics and Astronautics)	22	0.4—14.0	Water bodies, artificial targets, metal minerals

2.2 Distribution of ground substances

Based on the ground substance spectral reflectance images of known bands, the types and distribution of ground substances in the scene can be identified and inverted, and based on the accurate scene ground substance distribution, the ground substance spectral reflectance image of the unknown band of interest can be accurately reconstructed.

2.2.1 Ground substance classification and category identification

Through the ground substance classification, the types of ground substances in the ground substance spectral reflectance image can be determined. There are numerous types of ground substances in the image. Therefore, this paper uses Gaussian mixture clustering to perform the ground substance classification. The Gaussian mixture model[16] can accurately quantify ground substances and decompose a ground substance into several Gaussian probability density functions, representing different categories. It is a commonly used model to describe the mixture density distribution. Multiple optimizations are performed to calculate the probability distribution of each pixel in the image belonging to a certain substance category. When the probability density is the largest, the category is the "best" attribution of this pixel. The ground substance classification algorithm is as follows:

(1) Determine the number of categories S of the ground substance sample. After several experiments, this article sets $S=7$ and a certain sample as $s(s=1,2,\cdots,S)$.

(2) Determine the number of the Gaussian distributions Q. If the number is too large, it will lead to increased computational complexity and there is prone to overfitting. If the number is too small, it will lead to a reduction in classification accuracy. After experimentation, the number of Gaussian distributions used in this paper is set to $Q=5$, and a certain Gaussian distribution is $q(q=1,2,\cdots,Q)$.

(3) For each Gaussian distribution q, randomly assign the mean μ_q and variance σ_q.

(4) For each sample (every pixel x), calculate the probability belonging to each category of samples under each Gaussian distribution.

$$f(x)_s^q=\frac{1}{\sqrt{2\pi}\,\sigma_q}\exp\left(-\frac{(x-\mu_q)^2}{2\sigma_q^2}\right)\begin{matrix}s=1,2,\cdots,S\\ q=1,2,\cdots,Q\end{matrix} \tag{1}$$

(5) For each Gaussian distribution, the contribution of each sample (every pixel x) to the Gaussian distribution can be expressed by its probability $f(x)_s^q$. High probability means large contribution and vice versa. Take the contribution of the sample

to the Gaussian distribution $f(x)_s^q$ as a weight to calculate the new mean μ_q and variance σ_q of the Gaussian distribution by weighted sum of all samples (all pixels) to replace its original mean and variance.

(6) Repeat Steps (4) and (5) until the mean μ_q and variance σ_q of each Gaussian distribution converges.

(7) Use the converged mean μ_q and variance σ_q of each Gaussian distribution to calculate the probability $f(x)_s^q$ of each sample (each pixel x) belonging to various categories of samples under the Gaussian distribution. Obtain the mean of all Gaussian distributions and calculate the probability that a pixel x belongs to various categories of samples.

$$f(x)_s = \frac{1}{Q} f(x)_s^q \quad s = 1, 2, \cdots, S \tag{2}$$

(8) For each pixel x, classify it to the sample category corresponding to the maximum value of $f(x)_s$.

In this paper, the correlation distance is used to determine the categories of ground substances in the ground substances spectral reflectance image. The correlation distance is calculated between the spectral reflectance of a certain ground substance in the scene image and the spectral reflectance of each ground substance in the spectral reflectance database. When the value is the smallest, it is determined that the ground substance in the image is the corresponding ground substance in the spectral reflectance database that matches it. The correlation distance is shown as

$$d_{s,t} = 1 - \frac{\boldsymbol{X}_s \boldsymbol{X}_t'}{\sqrt{(\boldsymbol{X}_s - \bar{\boldsymbol{X}}_s)\cdot(\boldsymbol{X}_s - \bar{\boldsymbol{X}}_s)'} \cdot \sqrt{(\boldsymbol{X}_t - \bar{\boldsymbol{X}}_t)\cdot(\boldsymbol{X}_t - \bar{\boldsymbol{X}}_t)'}} \tag{3}$$

where $d_{s,t}$ is the correlation distance between the spectral reflectance vector of a certain type of ground substance in the image and the spectral reflectance vector of a type of ground substance in the spectral reflectance database; $\boldsymbol{X}_s$ the spectral reflectance vector of a certain type of ground substance in the image; $\bar{\boldsymbol{X}}_s$ the average value of $\boldsymbol{X}_s$; $\boldsymbol{X}_t$ the spectral reflectance vector of a certain type of ground substance in the spectral reflectance database, and $\bar{\boldsymbol{X}}_t$ the average value of $\boldsymbol{X}_t$.

2.2.2 Ground substance recognition

In addition to pure pixels, the ground substances' spectral reflectance image also contains mixed pixels where multiple ground substance categories coexist. In this paper, an image unmixing algorithm based on manifold space constraints[17] is used to calculate the proportion of different categories of the ground substances in each mixed pixel, that is, the abundance matrix.

The ground substance distribution of the spectral reflectance image is obtained from the abundance matrix of each pixel. By using the ground substance spectral reflectance of the band of interest in the ground substance spectral reflectance database, the ground substance spectral reflectance image of the band of interest can be accurately reconstructed, shown as

$$\boldsymbol{Y} = \boldsymbol{A}\boldsymbol{X} \tag{4}$$

where $\boldsymbol{Y} \in \mathbf{R}^n$ represents the ground substances spectral reflectance image of the band of interest and n the number of pixels; $\boldsymbol{A} \in \mathbf{R}^p$ represents the ground substances spectral reflectance data of the band of interest and p the types of the ground substances in the scene; $\boldsymbol{X} \in \mathbf{R}^{p \times n}$ represents the abundance matrix.

3 Inversion and Reconstruction of Ground Substance Temperature Field

The temperature field distribution is an intrinsic property of substance, which is determined by the type of substance and the thermal energy radiated by it. The low-resolution ground substance temperature field distribution in the scene can be inverted from the far-infrared image of the scene. Using this information, the high-resolution temperature field distribution of ground substances in the scene can be reconstructed through interpolation methods.

3.1 Inversion of low-resolution ground substance temperature field

The distribution of surface thermal energy can be extracted by the surface object temperature field. Therefore, it is feasible to invert the temperature

field of low-resolution ground substance temperature field through the low-resolution far-infrared image[18]. This paper uses the single-window algorithm proposed by Tan et al.[19], which is shown as

$$T_s=\frac{\left\{a(1-C-D)+\left[b(1-C-D)+C+D\right]T-D\cdot T_a\right\}}{C} \tag{5}$$

$$C=\varepsilon\cdot\tau \tag{6}$$

$$D=(1-\tau)\left[1+\tau\cdot(1-\varepsilon)\right] \tag{7}$$

$$T=\frac{K_2}{\ln\left(1+K_1/L_\lambda\right)} \tag{8}$$

where T_s is the ground substances temperature field; a, b are linear regression coefficients, where $a=-67.355\,351$, $b=0.458\,606$; T_a is the average temperature of the atmosphere, which can be calculated using empirical formula; T is the brightness temperature received by the detector; ε is the specific emissivity of the ground surface, which can be obtained by checking the table; τ is the atmospheric transmittance, which can be obtained by simulation using the Modtran software; L_λ is the spectral radiance of the far-infrared image; K_1, K_2 are both constants, determined before the detector payload is emitted, $K_1=774.89$ mW/(cm$^{-2}\cdot\mu$m$^{-1}\cdot$sr^{-1}) and $K_2=1\,321.08$ K[20].

In this paper, we select the far-infrared image of Nanjing Jiangning in August from the Landsat 8 data (10.9 μm band, 100 m resolution), and obtain the results of $T_a=16.011\,0+0.926\,21\times300$ based on the mid-latitudes-summer mode. The low-resolution ground substances temperature field distribution inverted by the single-window method is shown in Fig.2.

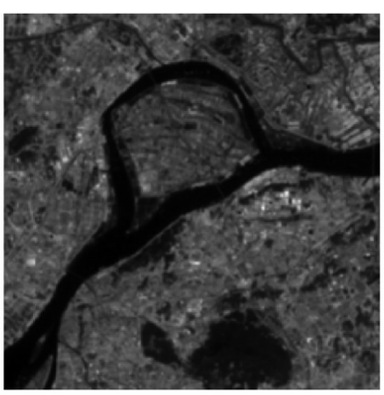

(a) Far-infrared image of Nanjing Jiangning in August

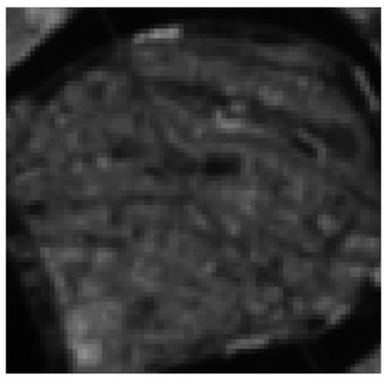

(b) Partially enlarged image of the far-infrared image

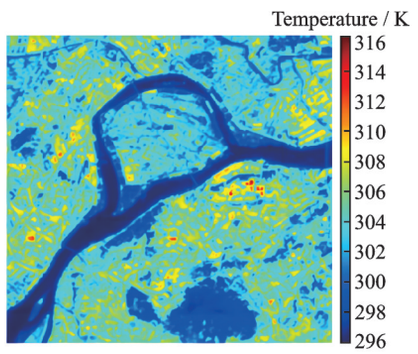

(c) Low-resolution ground substance temperature field distribution image

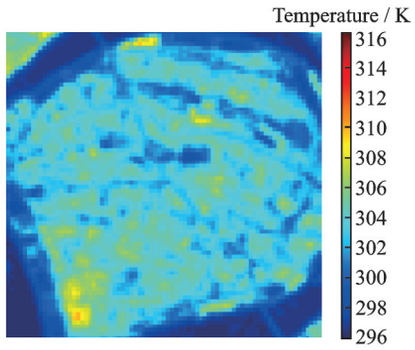

(d) Partially enlarged image of low-resolution ground substance temperature field distribution image

Fig.2 Landsat 8 far-infrared image and low-resolution ground substance temperature field distribution

3.2 Reconstruction of high-resolution ground substance temperature field

The continuous distribution of thermal energy radiated by ground substances allows for the reconstruction of the temperature field from low to high resolution using adjacent pixel interpolation. In this paper, the Shepard interpolation algorithm[21] is employed to interpolate the low-resolution temperature field distribution image of Nanjing Jiangning in August (Fig.2(c)) to a higher resolution, as depicted in Fig.3.

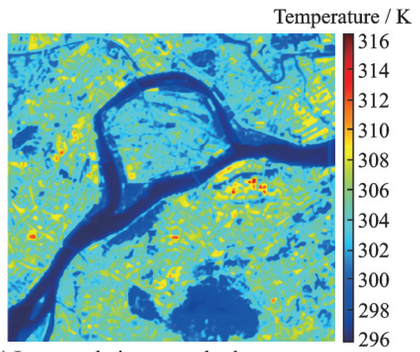

(a) Low-resolution ground substance temperature field distribution image

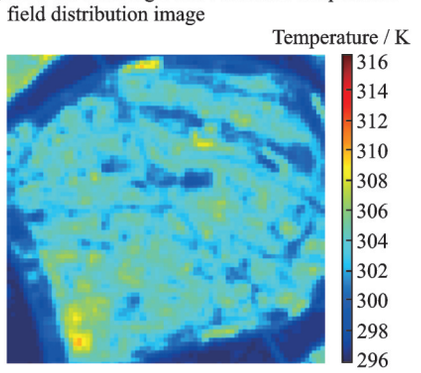

(b) Partially enlarged image of low-resolution ground substance temperature field distribution image

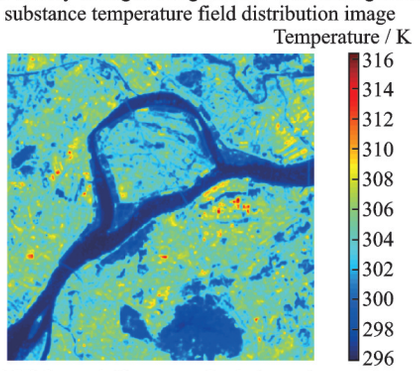

(c) High-resolution ground substance temperature field distribution image

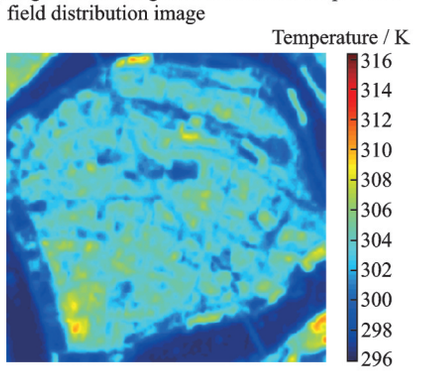

(d) Partially enlarged image of high-resolution ground substance temperature field distribution image

Fig.3 Reconstructed high-resolution ground substance temperature field distribution

4 Super-Resolution Inversion and Reconstruction of Unknown Infrared Band of Interest

Based on the distribution of ground substances in the scene, the spectral reflectance image of the interested unknown band is reconstructed by inversion. Specifically, this paper focuses on super-resolution reconstruction of the infrared band. By leveraging the high-resolution ground temperature field obtained from the reconstruction, we can accurately characterize the thermal energy radiated by the ground substances in the scene. This leads to a more comprehensive representation of the energy information of the ground substances, ultimately resulting in improved super-resolution accuracy of the unknown infrared band image of interest[22-24].

Schott[25] proposed a remote sensing link imaging model in 2007 that included light and thermal information of ground substances. In this paper, we utilize that model to super-resolution reconstruct the spectral radiance image of an unknown infrared band of interest, which can be represented by

$$L_\lambda = \{E'_{s\lambda}\cos\sigma' \cdot \tau_1(\lambda) \cdot \frac{r(\lambda)}{\pi} + \varepsilon(\lambda) \cdot L_{T\lambda} + F[E_{ds\lambda} + E_{d\varepsilon\lambda}]\frac{r_d(\lambda)}{\pi} + (1-F) \cdot [L_{bs\lambda} + L_{b\varepsilon\lambda}] \cdot r_d(\lambda)\} \cdot \tau_2(\lambda) + L_{us\lambda} + L_{ue\lambda} \quad (9)$$

where L_λ is the radiance of the remote sensing λ band received by the detector load; $E'_{s\lambda}$ the solar irradiance reaching the outer layer of the atmosphere, which is related to the azimuth of the sun; σ' the solar zenith angle; $r(\lambda)$ the spectral reflectance of ground substances in the λ band; $r_d(\lambda)$ the diffuse reflectance of ground substances; $\tau_1(\lambda)$ the atmospheric transmittance of the sun to the ground, $\tau_2(\lambda)$ the atmospheric transmittance of the ground to the detector load; F the sky shape parameter, and the value is within the range of 0—1; $\varepsilon(\lambda)$ the specific spectral emissivity of the ground substances; $L_{T\lambda}$ the spectral thermal radiation brightness of the ground substances at temperature T; $E_{ds\lambda}$ the irradiance of solar radiation scattered by the atmosphere and reflected by the ground; $E_{d\varepsilon\lambda}$ the radiation irradiance of the atmospheric downward thermal radiation reflected by the ground; $L_{bs\lambda}$ the radiation brightness of the sky background light reflected from the ground; $L_{b\varepsilon\lambda}$ the background thermal radiation brightness reflected from the ground; $L_{us\lambda}$ the radiation brightness of the sunlight scattered by the atmo-

sphere; $L_{u\varepsilon\lambda}$ the upward thermal radiation brightness of the atmosphere.

5 Experimental Results and Analysis

To evaluate the effectiveness of the proposed algorithm, Landsat 8 data is used for experiments. The experimental results are then compared with the 30 m-resolution far-infrared spectral radiance images super-resolution reconstructed by NASA, which are obtained from the official website of Earthexplorer. Extensive research is conducted but no literature or algorithm related to the research content is found. Therefore, no comparative experiment is included in this paper. The proposed algorithm's robustness is verified through multiple experiments on various scene images of Landsat 8.

All experimental results are obtained on the same platform and hardware conditions. Experimental environment: Matlab 2016. Experimental platform: 3.60 GHz, Intel i7 processor, 64-bit Win 7 operating system, 8 GB memory.

5.1 Experimental data

In this paper, the super-resolution inversion reconstruction algorithm is used to calculate the space-based remote sensing image, which requires the existence of multi-spectral image and at least one far-infrared band image in the original data. At the same time, in order to verify the robustness of the proposed algorithm, a large number of original data for different scenes are needed for experimentation. In view of it, this paper uses the Landsat 8 satellite data published by NASA for experiments. Landsat 8 data includes spectral images across 9 visible light to near-infrared bands and 2 far-infrared bands, encompassing a broad range that fulfills the experimental requirements of this study.

This paper takes two images of the Landsat 8 satellite data as examples, as shown in Fig.4. These two images are true color images of the B4, B3, and B2 bands of two different scenes in the Nanjing area on 2014-06-11. The center wavelength and spatial resolution of each spectral band of these two images are listed in Table 2, and the data description is listed in Table 3. The input data for this study includes B1, B2, B3, B4, B5, B6, B7, and B10 band images, while the unknown band of interest for inversion reconstruction is B11 (far-infrared).

(a) Natural environment scene (b) Urban hydrological scene

Fig.4 Landsat 8 satellite true color images of B4, B3, and B2 bands in two different scenes

Table 2 Landsat 8 satellite center wavelength and spatial resolution

Band	B1	B2	B3	B4	B5	B6	B7	B8	B9	B10	B11
Center wavelength/μm	0.443	0.482 5	0.562 5	0.655	0.865	1.61	2.2	0.64	1.35	10.9	12.0
Spatial resolution/m	30	30	30	30	30	30	30	15	30	100	100

Table 3 Description of the image data of two different scenes

Scene	Resolution/m	Scene location	Scene characteristics
Natural environment	30/100	Nanjing, Jiangsu Province, China	The natural environment is dominant, including typical natural scenes such as woodland, grassland, and rivers
Urban hydrological	30/100	Nanjing, Jiangsu Province, China	The urban environment is dominant, including urban buildings and some hydrological scenes

5.2 Evaluation index of experimental results

This paper utilizes widely recognized quality evaluation indicators, namely signal reconstruction error (SRE), peak signal-to-noise ratio (PSNR), and structural similarity index measure (SSIM), to assess the image quality of the inverted reconstruct-

ed super-resolution algorithms. The SRE is calculated in dB and is derived from the reconstructed image $\hat{\boldsymbol{H}}$ and the scene ground truth $\boldsymbol{H}$, as shown in Eq.(10). A larger SRE indicates a smaller reconstruction error and a higher reconstruction accuracy.

$$\mathrm{SRE}=10\lg\frac{\mu_H^2}{\left\|\boldsymbol{H}-\hat{\boldsymbol{H}}\right\|^2/l} \tag{10}$$

where SRE is the signal reconstruction error, $\boldsymbol{H}$ the scene ground truth, $\hat{\boldsymbol{H}}$ the super-resolution reconstructed image, l the number of bands of the input image, and μ_H the average of $\boldsymbol{H}$.

As PSNR increases, the quality of the super-resolution reconstructed image[25] and the reconstruction accuracy also improve, as demonstrated by

$$\mathrm{MSE}=\frac{1}{M\times N}\left\|\boldsymbol{H}-\hat{\boldsymbol{H}}\right\|^2 \tag{11}$$

$$\mathrm{PSNR}=10\times\lg\left(\frac{L^2}{\mathrm{MSE}}\right) \tag{12}$$

where MSE is mean-square error; $\boldsymbol{H}$ the scene ground truth; $\hat{\boldsymbol{H}}$ the super-resolution reconstructed image; M and N are the height and width of the image, respectively; L the largest gray value in the gray level, and here $L=255$.

The value of SSIM ranges from -1 to 1. The closer the SSIM is to 1, the closer the super-resolution reconstructed image is to the real image. It is shown as

$$\mathrm{SSIM}(\hat{\boldsymbol{H}},\boldsymbol{H})=\frac{(2\mu_{\hat{H}}\mu_H+C_1)(2\sigma_{\hat{H}H}+C_2)}{(\mu_{\hat{H}}^2+\mu_H^2+C_1)(\sigma_{\hat{H}}^2+\sigma_H^2+C_2)} \tag{13}$$

$$C_1=(k_1L)^2 \tag{14}$$

$$C_2=(k_2L)^2 \tag{15}$$

where $\mu_{\hat{H}}$, μ_H, $\sigma_{\hat{H}}$, σ_H and $\sigma_{\hat{H}H}$ are the mean, standard deviation and mutual covariance of $\hat{\boldsymbol{H}}$ and $\boldsymbol{H}$, respectively; k_1 and k_2 are constants, generally taken as $k_1=0.01$ and $k_2=0.03$.

5.3 Algorithm effectiveness experiment

This paper uses two images from Landsat 8 satellite data as examples to analyze and illustrate the experimental results. These images depict different scenes in the Nanjing area on June 11, 2014. The first scene represents a natural environment, while the second scene portrays an urban hydrological landscape. In this paper, the B11 band (far-infrared) is the unknown band of interest to be inversion reconstructed. The B1, B2, B3, B4, B5, B6, and B7 band images are used as input data to invert and reconstruct the ground substance spectral reflectance image. The B10 band image is used as input data to invert and reconstruct the high-resolution ground substance temperature field distribution image. Based on the ground substance spectral reflectance image and the ground substance temperature field distribution image, the high-resolution infrared image (30 m resolution) of unknown B11 band of interest is inversion reconstructed. The SRE and PSNR are used as the quality evaluation indexes of the super-resolution inversion reconstructed image.

5.3.1 Experiments in a natural environment scene

Experimental results for super-resolution inversion and reconstruction of a representative natural environment scene are depicted in Fig. 5. In Figs. 5 (a,b), the infrared radiation brightness value is represented by pseudo color from dark blue to dark red, which corresponds to brightness values from

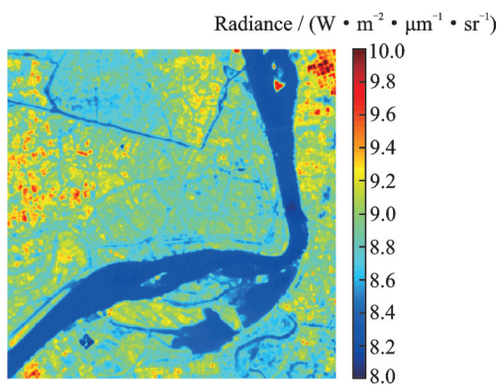

(a) NASA super-resolution B11 band infrared radiation image downloaded from the Earthexplorer official website

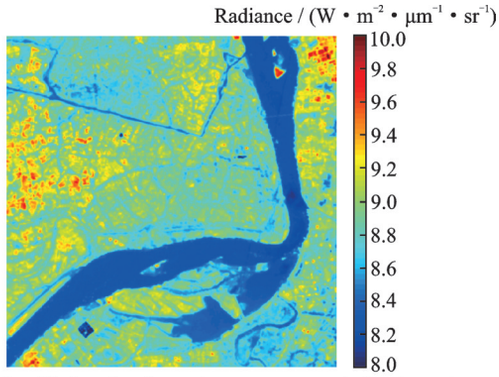

(b) B11 band infrared radiance image super-resolution inversion reconstructed by the proposed algorithm

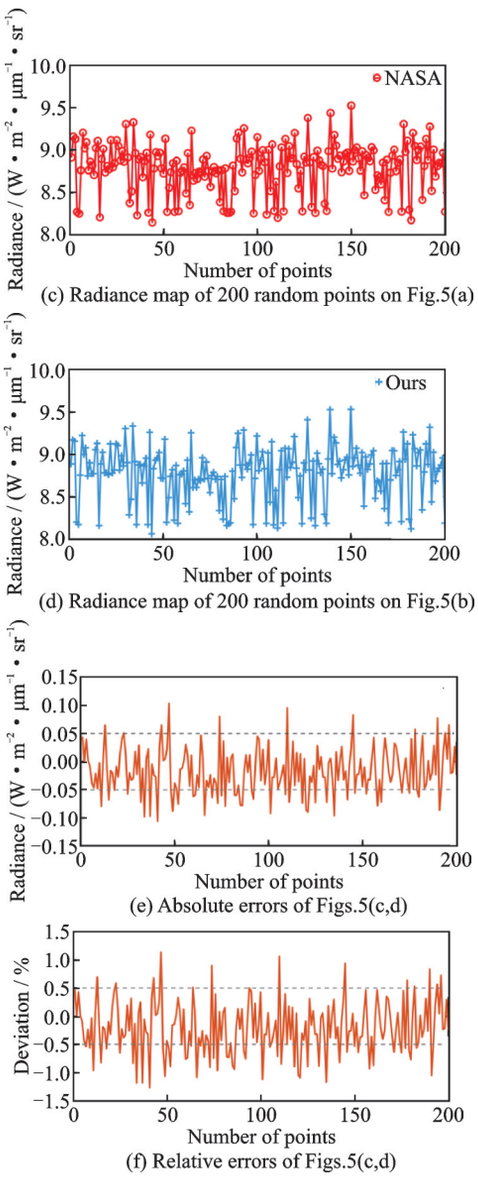

Fig.5 Comparison of experimental results of super-resolution inversion and reconstruction of natural environment scenes

low to high. Figs.5(a,b) show the same overall contours and geometric shapes, and the color distribution is basically the same, indicating that the infrared radiation brightness distributions of the two images are basically the same. For example, in Fig.5(a), there is a large continuous dark blue area from the lower left to the upper right, a red-yellow area on the left side of the image, a blue-green area with a light blue lines and light yellow patches in the middle of the image, a dense crimson area in the upper right corner, and a blue-green area with many continuous short light blue lines interspersed with light yellow patches in the lower right corner. In Fig.5(b), the above-mentioned areas are basically consistent with those in Fig.5(a). This shows that the infrared radiation brightness distributions of the two images maintain a high degree of consistency.

The curves in Figs.5(c, d) exhibit similar shapes and value distributions, indicating comparable infrared radiation brightness distributions of the two images. In Fig.5(e), the absolute errors of Figs.5(c,d) fall within the range [−0.1, 0.1], primarily concentrated between [−0.05, 0.05], with a few exceptions beyond [−0.1, 0.1], but none exceeding 0.15. Fig.5(f) demonstrates that the relative errors of Figs.5(c,d) are distributed between [−1%, 1%], mostly concentrated within [−0.5%, 0.5%], with only a few points outside [−1%, 1%], but none reaching 1.5%. Thus, the infrared radiation brightness distributions of the two images are highly consistent.

The experiment results demonstrate that the algorithm effectively reconstructs the super-resolution B11 band infrared radiance image. It exhibits a strong consistency with the NASA super-resolution B11 band infrared radiance image obtained from the official website of Earthexplorer. The algorithm is particularly efficient in enhancing the resolution of natural environment scenes, including water bodies, grasslands, forests, and soil.

5.3.2 Experiments in an urban hydrological scene

The super-resolution inversion and reconstruction results of an urban hydrological scene are depicted in Fig.6.

In Figs.6(a, b), the infrared radiation brightness value is represented by pseudo color from dark

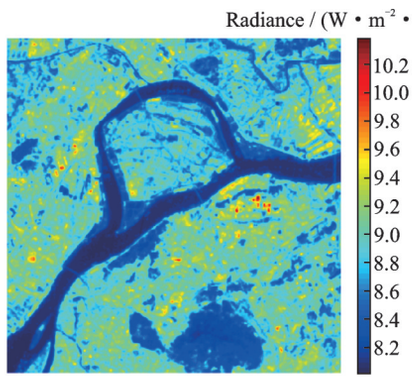

(a) NASA super-resolution B11 band infrared radiation image downloaded from the Earthexplorer official website

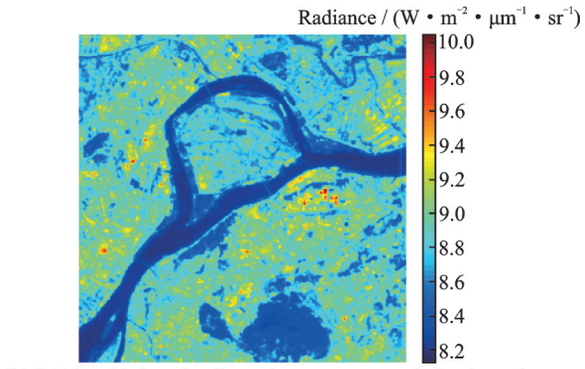

(b) B11 band infrared radiance image super-resolution inversion reconstructed by the proposed algorithm

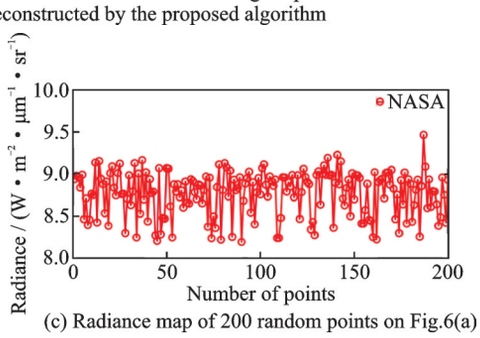

(c) Radiance map of 200 random points on Fig.6(a)

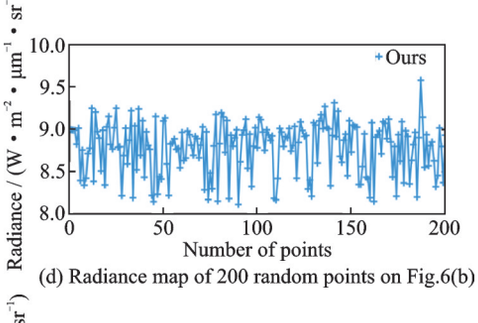

(d) Radiance map of 200 random points on Fig.6(b)

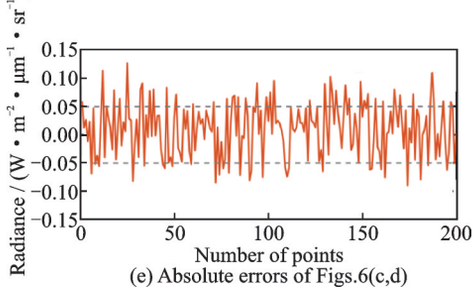

(e) Absolute errors of Figs.6(c,d)

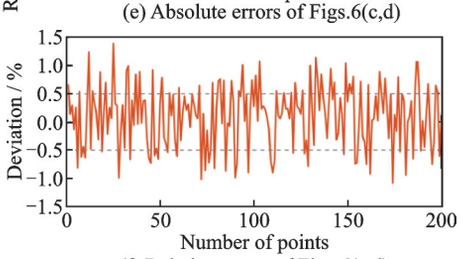

(f) Relative errors of Figs.6(c,d)

Fig.6 Comparison of experimental results of super-resolution inversion and reconstruction of urban hydrological scenes

blue to dark red, which corresponds to brightness values from low to high. Figs.6(a,b) have the same overall contours and geometric shapes, and the color distributions are basically the same, indicating that the infrared radiation brightness distributions of the two images are basically the same. For example, in Fig.6(a), there are large continuous dark blue areas from the lower left to the upper right as well as in the middle and lower parts of the image. Especially, in the middle of the image, there is a light blue rectangular shaped area surrounded by a dark blue area and interspersed with dark blue lines. At the lower right side of this rectangular area, there is a blue-green area interspersed by a large number of small yellow areas and some red areas. At the left side of the rectangular area, there are small yellow areas and red areas interspersed by some dark blue lines. At the upper right side of the rectangular area, there are many continuous light blue lines, as well as a large number of densely distributed short light blue lines, with small yellow blocks in between. In Fig.6(b), the above-mentioned areas are substantially the same as those in Fig.6(a). Therefore, it can be concluded that the infrared radiation brightness distributions in the two images exhibit a high level of consistency.

Figs.6(c,d) show similar curve shapes and numerical distributions, indicating that the infrared radiation brightness distributions of the two images are similar. In Fig.6(e), the absolute errors of Figs.6(c,d) lie within the range [−0.1, 0.1], with the majority falling within [−0.05, 0.05]. A few points fall outside the range but none exceeds 0.15. In Fig.6(f), the relative errors of Figs.6(c,d) are distributed within [−1%, 1%], with the majority falling within [−0.5%, 0.5%]. A few points fall outside the range but none exceeds 1.5%. This implies a high level of consistency in the infrared radiation brightness distributions of the two images.

Experimental results show that the super-resolution B11 band infrared radiance image inverted and reconstructed by the proposed algorithm maintains high consistency with the NASA super-resolution B11 band infrared radiance image downloaded from the Earthexplorer's official website. The proposed algorithm effectively enhances and reconstructs urban hydrological scene images, particularly improving resolution for water sources, concrete buildings, and asphalt roads.

5.3.3 Algorithm effectiveness evaluation

The quality of the super-resolution inversion reconstructed images is evaluated using the signal reconstruction error, peak signal-to-noise ratio, and structural similarity index measure. Table 4 displays the calculated indexes of the super-resolution B11 band infrared radiance brightness images in two scenes: The natural environment and the urban hydrological scene.

Table 4 Quality evaluation of super-resolution inversion reconstructed images

Scene	SRE /dB	PSNR/ dB	SSIM
Natural environment	33.25	70.39	0.957 4
Urban hydrological	35.45	76.69	0.960 7

From Table 4, it can be observed that the SRE values are higher than 25, the PSNR values are higher than 55 and the SSIM values are higher than 0.9, indicating that the similarity between the reconstructed image and the original scene image is very high. Specifically, Table 4 shows that the SRE values of the super-resolution inversion reconstructed images of the natural environment scene and the urban hydrological scene are 8.25 and 10.45 higher than 25, respectively; the PSNR values are 15.39 and 21.69 higher than 55, respectively; the SSIM values are 0.057 4 and 0.060 7 higher than 0.9, respectively. This paper presents super-resolution inversion reconstructed images that exhibit a significant resemblance to the original scene image. These results validate the algorithm's efficacy.

5.4 Algorithm robustness experiment

This paper conducts multiple experiments on various scenes from Landsat 8 to validate the algorithm's robustness. Five different scenes are taken as examples, and the calculation results for the quality evaluation indices, namely SRE, PSNR and SSIM, of the super-resolution B11 band infrared radiation brightness images are presented in Table 5 and Fig.7.

Based on Table 5 and Fig.7, the SRE values exceed 25, PSNR values exceed 55, and SSIM values exceed 0.9, indicating a significant similarity between the reconstructed image and the original scene image. Specifically, Table 5 and Fig.7 show that the SRE values of the super-resolution inversion reconstructed images of five different scenes are 5.25, 12.13, 8.68, 6.08, and 9.61 higher than 25, respectively; the PSNR values are 13.45, 24.89, 19.35, 16.36, and 20.26 higher than 55, respectively; the SSIM values are 0.030 4, 0.058 1, 0.055 5, 0.045 9, and 0.056 0 higher than 0.9, respectively. The super-resolution inversion reconstructed images in this paper show a high similarity with the original scene image. Table 5 and Fig.7 demonstrate that the SRE values of the super-resolution inversion reconstructed images of five different scenes are all above 30, ranging between 30.25 and 37.13. The average SRE value is 33.35 with a fluctuation range of −3.10 to 3.78. The PSNR values are all above 68, ranging from 68.45 to 79.89, with an average value of 73.86 and a fluctuation range of −5.41 to 6.03. Similarly, the SSIM values are all above 0.93, ranging from 0.930 4 to 0.958 1, with an average value of 0.949 2 and a fluctuation range of

Table 5 Quality evaluation of super-resolution inversion reconstructed images of five different scenes

Scene	SRE/dB	PSNR/dB	SSIM
1	30.25	68.45	0.930 4
2	37.13	79.89	0.958 1
3	33.68	74.35	0.945 9
4	31.08	71.36	0.955 5
5	34.61	75.26	0.956 0

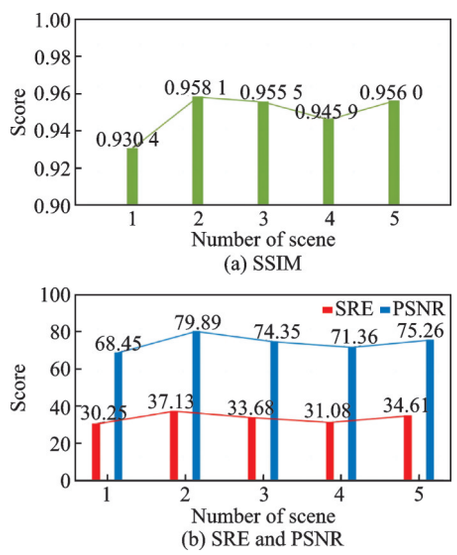

Fig.7 Quality evaluation indexes of super-resolution inversion reconstructed images of five different scenes

−0.018 8 to 0.008 9. Therefore, the proposed algorithm has good robustness.

6 Conclusions

The algorithm in this paper utilizes both light energy and thermal energy information from ground substances to better characterize the energy information in the scene, resulting in improved accuracy in super-resolution of unknown infrared band images. Experimental results indicate that the proposed algorithm effectively reconstructs high-resolution remote sensing images in an unknown infrared band. The reconstructed image closely resembles the original scene, thereby enhancing the capacity for target detection and recognition.

In this paper, the ground is regarded as a simple and uniform Lambert body in the study of super resolution inversion reconstruction of remote sensing image of fine spectrum, and the bidirectional reflection distribution function (BRDF) is not considered when the ground is non-uniform. Therefore, a crucial research direction and target for future studies is to incorporate the BRDF of substance.

References

[1] XU Hong. Research on key technologies of multispectral and hyperspectral imaging detection[D]. Tianjin: Tianjin University, 2009.(in Chinese)

[2] SINGH S, KALRA M K, HSIEH J, et al. Abdominal CT: Comparison of adaptive statistical iterative and filtered back projection reconstruction techniques[J]. International Journal of Medical Radiology, 2011,257(2): 373-383.

[3] TANG Z, DENG M, XIAO C, et al. Projection onto convex sets super-resolution image reconstruction based on wavelet bi-cubic interpolation[C]//Proceedings of International Conference on Electronic and Mechanical Engineering and Information Technology. Harbin, China: IEEE, 2011: 351-354.

[4] XU J, ZHANG L, ZUO W, et al. Patch group based nonlocal self-similarity prior learning for image denoising[C]//Proceedings of the IEEE International Conference on Learning Computer Vision. Chile: IEEE, 2015: 244-252.

[5] CAO F, CAI M, TAN Y, et al. Image super-resolution via adaptive regularization and sparse representation[J]. IEEE Transactions on Neural Networks and Learning Systems, 2016, 27(7): 1550-1561.

[6] NAZREN A R A, YAAKOB S N, NGADIRAN R, et al. Improving iterative back projection super resolution model via anisotropic diffusion edge enhancement[C]//Proceedings of International Conference on Robotics, Automation and Sciences. Ayer Keroh, Malaysia: IEEE, 2017: 1-4.

[7] LIU J, YANG W, ZHANG X, et al. Retrieval compensated group structured sparsity for image super-resolution[J]. IEEE Transactions on Multimedia, 2017, 19(2): 302-316.

[8] HUANG S, SUN J, YANG Y, et al. Robust single-image super-resolution based on adaptive edge-preserving smoothing regularization[J]. IEEE Transactions on Image Processing, 2018, 27(6): 2650-2663.

[9] ZHANG Y, TIAN Y, KONG Y, et al. Residual dense network for image super-resolution[C]//Proceedings of the IEEE/CVF Conference on Computer Vision and Pattern Recognition (CVPR). Salt Lake City, Utah, USA: IEEE, 2018: 2472-2481.

[10] GAO S, ZHUANG X. Multi-scale deep neural networks for real image super resolution[C]//Proceedings of the IEEE/CVF Conference on Computer Vision and Pattern Recognition Workshops (CVPRW). Long Beach, USA: IEEE, 2019: 2006-2013.

[11] JIANG K, WANG Z, YI P, et al. Edge-enhanced GAN for remote sensing image superresolution[J]. IEEE Transactions on Geoscience and Remote Sensing, 2019,57(8): 5799-5812.

[12] XIAO Y, SU X, YUAN Q, et al. Satellite video super-resolution via multiscale deformable convolution alignment and temporal grouping projection[J]. IEEE Transactions on Geoscience and Remote Sensing, 2021,60(9): 5610819.

[13] XIAO Y, YUAN Q, HE J. Space-time super-resolution for satellite video: A joint framework based on multi-scale spatial-temporal transformer[J]. International Journal of Applied Earth Observation and Geoinformation, 2022,108(4): 102731.

[14] WANG Zhangye. Infrared imaging simulation of ground targets and realistic fusion of multispectral imaging[D]. Hangzhou: Zhejiang University, 2002: 85-97.(in Chinese)

[15] ZHANG Kun. Study on spectral demixing and end-element extraction of hyperspectral images[D]. Xi'an: Chang'an University, 2016: 9-19.(in Chinese)

[16] LU M, SUN J. Moving image target detection algorithm based on improved Gaussian mixture model[J]. Optoelectronic Technology and Application, 2019,40(6): 874-879.

[17] YAN J, HUANG W, ZHANG Y. Spatial constrained hyperspectral image demixing algorithm[J].

Journal of Instrumentation, 2019,40(3): 188-194.
[18] LI J, GONG W, XIN X, et al. Remote sensing inversion and spatial differentiation of surface temperature in Chongqing[J]. Remote Sensing Technology and Application, 2018, 33(5): 820-828.
[19] TAN Z, ZHANG M H, KARNIELI A. Single-window algorithm for calculating surface temperature using land satellite TM6 data[J]. Acta Geographica Sinica, 2001(4): 456-466.
[20] ZHU X, YANG Y, LI X, et al. Research on Landsat8 land surface temperature inversion algorithm[J]. Geospatial Information, 2018,16(9): 103-106.
[21] YANG Yuxiang. Research on image super-resolution reconstruction algorithm[D]. Hefei: University of Science and Technology of China, 2013: 14-17.(in Chinese)
[22] SU Q, YANG J, WANG Y. Synthetic aperture radar image change detection based on intuitionistic fuzzy C kernel mean clustering algorithm[J]. Progress in Laser and Optoelectronics, 2019, 56(19): 1-7.
[23] JIA Meng. Remote sensing image change detection and classification based on spatial information and statistical learning[D]. Xi'an: Xidian University, 2016: 55-68.(in Chinese)
[24] SONG Guolei. Research on hybrid fuzzy water and land segmentation algorithm based on SAR image—Taking Danjiangkou Reservoir as an example[D]. Changsha: Hunan University, 2017: 30-34.(in Chinese)
[25] SCHOTT J R. Remote sensing: The image chain approach[M]. 2nd ed. Oxford: Oxford University Press, 2007: 57-108.

Acknowledgements This work was supported by the National Defense Science and Technology Foundation Strengthening Program (No. 2021-JCJQ-JJ-0834), and the Fundamental Research Funds for the Central Universities (Nos.NJ2022025, NP2022450).

Author Prof. **YAN Junhua** received her B.S., M.S., and Ph.D. degrees from Nanjing University of Aeronautics and Astronautics in 1993, 2001, and 2004, respectively. She is a professor at Nanjing University of Aeronautics and Astronautics. She is the author of more than 60 journal papers and has 12 patents. Her current research interests include image super-resolution reconstruction, multisource information fusion, target detection, tracking, and recognition.

Author contributions Prof. **YAN Junhua** designed the study, complied the models and wrote the manuscript. Mr. **YU Liqian** contributed to data analysis, results interpretation and manuscript revision. Mr. **XIA Chongxiang** contributed to the discussion and revision of the study. Mr. **ZHANG Qiqi** contributed to the experiment analysis. Mr. **XU Zhenyu** contributed to the design and discussion of the study. Dr. **ZHANG Yin** contributed to the discussion and background of the study. Mr. **FAN Junjie** contributed to the review and revision of the draft. All authors commented on the manuscript draft and approved the submission.

Competing interests The authors declare no competing interests.

(Production Editor: WANG Jing)

感兴趣未知红外波段遥感图像超分辨率反演重构

闫钧华[1,2], 俞立谦[1,2], 夏翀翔[1,2], 章琪琪[1,2], 许祯瑜[1,2], 张 寅[1,2], 范君杰[1,2]

(1.工业和信息化部空间光电探测与感知重点实验室(南京航空航天大学),南京 211106,中国;
2.南京航空航天大学航天学院,南京 211106,中国)

摘要:提出了感兴趣未知波段遥感图像超分辨率反演重构算法。基于已有波段的多光谱图像,根据构建的地物光谱反射率数据库,利用高斯混合聚类算法和相关距离法,对辐射定标和大气校正后的场景光谱反射率图像的物质进行分类与类别判定。基于流形空间约束的图像解混算法得到场景图像的地物分布,据此,反演重构感兴趣未知波段地物光谱反射率图像。基于已有波段的远红外图像,利用温度反演算法与插值算法,反演重构感兴趣未知波段高分辨率地物温度场分布。根据地物光谱反射率信息和地物温度场信息,利用遥感链路成像模型,超分辨率反演重构出感兴趣未知红外波段高分辨率遥感图像。实验结果表明,本文算法能够超分辨率反演重构出感兴趣未知红外波段不同场景的高分辨率遥感图像,重构图像与场景实况图像的相似度很高,提升图像的目标检测识别能力。

关键词:超分辨率反演重构;遥感图像;地物分布;光谱反射率字典;温度场反演重构